Discovery of Two Einstein Crosses from Massive Post-blue Nugget Galaxies at z > 1 in KiDS[*]

N. R. Napolitano[1] , R. Li[1] , C. Spiniello[2,3] , C. Tortora[3,4] , A. Sergeyev[5,6] , G. D'Ago[7] , X. Guo[8,9] , L. Xie[1] ,
M. Radovich[10] , N. Roy[1], L. V. E. Koopmans[11] , K. Kuijken[12] , M. Bilicki[13] , T. Erben[14], F. Getman[15], C. Heymans[16,17] ,
H. Hildebrandt[17], C. Moya[7] , H. Y. Shan[18,19] , G. Vernardos[20], and A. H. Wright[21]

[1] School of Physics and Astronomy, Sun Yat-sen University Zhuhai Campus, Daxue Road 2, 519082–Tangjia, Zhuhai, Guangdong, People's Republic of China; lirui228@mail.sysu.edu.cn
[2] Department of Physics, University of Oxford, Denys Wilkinson Building, Keble Road, Oxford OX1 3RH, UK
[3] INAFOsservatorio Astronomico di Capodimonte, Salita Moiariello 16, I-80131Napoli, Italy
[4] INAF–Osservatorio Astronomico di Arcetri, L.go E. Fermi 5, I-50125–Firenze, Italy
[5] Institute of Astronomy, V. N. Karazin Kharkiv National University, 35 Sumska Str., Kharkiv, Ukraine
[6] Institute of Radio Astronomy of the National Academy of Sciences of Ukraine, Ukraine
[7] Instituto de Astrofísica, Pontificia Universidad Católica de Chile, Av. Vicuña Mackenna 4860, 7820436 Macul, Santiago, Chile
[8] School of Astronomy and Space Science, Nanjing University, Nanjing, Jiangsu 210093, People's Republic of China
[9] Key Laboratory of Modern Astronomy and Astrophysics (Nanjing University), Ministry of Education, Nanjing 210093, People's Republic of China
[10] INAF—Osservatorio Astronomico di Padova, vicolo dell'Osservatorio 5, I-35122 Padova, Italy
[11] Kapteyn Astronomical Institute, University of Groningen, P.O. Box 800, 9700AV Groningen, The Netherlands
[12] Leiden Observatory, Leiden University, P.O. Box 9513, 2300RA Leiden, The Netherlands
[13] Center for Theoretical Physics, Polish Academy of Sciences, al. Lotników 32/46, 02-668, Warsaw, Poland
[14] Argelander-Institut für Astronomie, Auf dem Hügel 71, D-53121 Bonn / Germany
[15] INAF—Astronomical Observatory of Capodimonte, Via Moiariello 16, 80131 Napoli, Italy
[16] Institute for Astronomy, University of Edinburgh, Royal Observatory, Blackford Hill, Edinburgh, EH9 3HJ, UK
[17] Ruhr-University Bochum, Astronomical Institute, German Centre for Cosmological Lensing, Universitätsstr. 150, D-44801 Bochum, Germany
[18] Shanghai Astronomical Observatory (SHAO), Nandan Road 80, Shanghai 200030, People's Republic of China
[19] University of Chinese Academy of Sciences, Beijing 100049, People's Republic of China
[20] Institute of Astrophysics, Foundation for Research and Technology− Hellas (FORTH), GR-70013, Heraklion, Greece
[21] Astronomisches Institut, Ruhr-Universität Bochum, Universitätsstr. 150, D-44780 Bochum, Germany

Abstract

We report the discovery of two Einstein Crosses (ECs) in the footprint of the Kilo-Degree Survey (KiDS): KIDS J232940-340922 and KIDS J122456+005048. Using integral field spectroscopy from the Multi Unit Spectroscopic Explorer at the Very Large Telescope, we confirm their gravitational-lens nature. In both cases, the four spectra of the source clearly show a prominence of absorption features, hence revealing an evolved stellar population with little star formation. The lensing model of the two systems, assuming a singular isothermal ellipsoid (SIE) with external shear, shows that: (1) the two crosses, located at redshift $z = 0.38$ and 0.24, have Einstein radius $R_{\rm E} = 5.2$ kpc and 5.4 kpc, respectively; (2) their projected dark matter fractions inside the half effective radius 0.60 and 0.56 (Chabrier initial mass function); (3) the sources are ultra-compact galaxies, $R_{\rm e} \sim 0.9$ kpc (at redshift, $z_{\rm s} = 1.59$) and $R_{\rm e} \sim 0.5$ kpc ($z_{\rm s} = 1.10$), respectively. These results are unaffected by the underlying mass density assumption. Due to size, blue color, and absorption-dominated spectra, corroborated by low specific star formation rates derived from optical–near-infrared spectral energy distribution fitting, we argue that the two lensed sources in these ECs are blue nuggets migrating toward their quenching phase.

Unified Astronomy Thesaurus concepts: Gravitational lensing (670); Strong gravitational lensing (1643); Galaxy formation (595); Dark matter (353)

1. Introduction

Strong gravitational lensing is a powerful tool to measure the distribution of dark matter (DM) in galaxies and study the properties of high-redshift sources. According to General Relativity, matter in the universe acts as a cosmic telescope deforming and magnifying the light of objects that would be hardly observable otherwise. Depending on the size of the source and the alignment of the foreground galaxy (lens or deflector) and the source, strong lensing events show up as arcs or rings (when the source is extended, e.g., a galaxy) or as multiple images (when the source is a compact system, e.g., a quasar). Deformed images of background galaxies can be used, in combination with the dynamical and stellar population

analysis of the deflector, to determine the lens total mass density profiles (e.g., Koopmans et al. 2006; Auger et al. 2010; Nightingale et al. 2019), to separate the dark from the luminous matter and to constrain the lens stellar initial mass-function (IMF) slope (e.g., Treu et al. 2010; Spiniello et al. 2011). Furthermore, doubly ("doublets") or even quadruply lensed ("quads") quasi-stellar objects (QSOs) are particularly valuable for cosmology because they enable measuring the Hubble constant (H_0, Suyu et al. 2013) via time-delays among the QSO light curves.

However, doublets and quads can also be produced by other compact sources, e.g., high-redshift, star-forming, ultra-compact galaxies (e.g., Muzzin et al. 2012, which are fairly common at high-z. Using lensing forecasts from typical ground-based surveys (Collett 2015) with a depth of the order of $r \sim 25$, the number of expected quads from compact

galaxies ($R_e < 1$ kpc) at redshift $z \lesssim 4$, with an alignment sufficient to make a cross-like geometry (e.g., source misalignment $<0''.1$), is of the order of half a dozen every 1000 deg^2 (see also Section 4). Unfortunately, to date only a few such systems have been observed: aside from the Muzzin et al. (2012) system, only two Einstein Cross (EC) configurations from Ly-α emitters have been confirmed and fully analyzed (Bolton et al. 2006; Bettoni et al. 2019). ECs are interesting per se as they are the rarest and most spectacular manifestation of quad systems, showing a distinctive symmetric cross pattern around the deflector, generated when the source and the lens are almost perfectly aligned. Generally, these systems have been found to be produced by distant quasars (e.g., Magain et al. 1988; Ostrovski et al. 2018) or supernovae (also known as Refsdal systems; Kelly et al. 2015).

Within the Kilo-Degree Survey (KiDS; de Jong et al. 2013), we have undertaken a systematic search for strong gravitational lenses, both arcs (Petrillo et al. 2017, hereafter P+17; Petrillo et al. 2019b, 2019a) and multiple images (Spiniello et al. 2018, 2019). In particular, in the process of improving the overall efficiency of the convolutional neural network (CNN) finders, started with P+17, we have collected, in an area of $\sim 1000 \text{deg}^2$, a series of high-quality quad candidates (Li et al. 2020, hereafter Li+20), among which we found three clear EC configurations.

In this Letter we report the results of the spectroscopic follow up of the two best examples of these EC configurations. We argue that these represent a new class of sources of EC configurations, i.e., high-z post-blue nugget systems, and discuss the possibility of systematically searching for these objects in current and future ground- and space-based surveys. For all calculations, we assume a ΛCDM cosmology with $(\Omega_M, \Omega_\Lambda, h) = (0.3, 0.7, 0.7)$.

2. Confirmation and Lensing Model

The first EC, KIDS J232940-340922 (hereafter KIDS-EC1; see Figure 1), has been found in the Southern KiDS patch. The deflector has an AB magnitude of $r \sim 19.8$ and red color, $g - i = 1.4$, while the average magnitude of the four lensed images of the source is $r \sim 22.6$ and their average color is $g - i = -0.21$. The second EC, KIDS J122456+005048 (hereafter KIDS-EC2; see Figure 1), has been found in the Northern KiDS patch. The deflector has total magnitude $r \sim 19.7$ and color $g - i = 1.9$, while the four images have an average magnitude $r \sim 22.0$ and average color $g - i = 1.0$, i.e., bluer than the deflector but redder than the KIDS-EC1 source. The two sources have obtained a high CNN probability and also high human visual score (see Li+20), hence they have been selected for the spectroscopic follow up. Table 1 lists coordinates, the relative positions of the lenses, and source images and the optical and near-infrared (NIR) photometry in the *ugriZYJHK*$_s$ bands, for both ECs. To minimize the relative contamination and derive homogeneous photometry for all sources, the nine-band photometry of the lenses and lensed images are derived by a simultaneous seeing convolved Sérsic plus 2D Gaussian fit of the objects, respectively, from KiDS-DR4 (Kuijken et al. 2019) and VIKING (Edge et al. 2013) calibrated images.

2.1. MUSE Spectroscopy and Lensing Confirmation

Spectroscopic observations have been collected under ESO Directory Discretionary Time (program ID: 0105.A-0253, PI Napolitano) with Multi Unit Spectroscopic Explorer (MUSE) at the Very Large Telescope (VLT), Cerro Paranal. Run A was completed in December 2019 for KIDS J232940-340922 and Run B on February 2020 for KIDS J122456+005048. Observations have been taken in service mode, in wide-field non-adaptive optic configuration, which allows a full $1' \times 1'$ field of view (FOV), in the wavelength range $\lambda = [4750, 9300]$Å. The MUSE grating spectral resolution varies from 1750 to 3750, end-to-end, in the same interval. The total exposure time for both targets is 130 minutes divided in three observing blocks (OBs). Every OB is split in 2×1300 s exposures with a 90deg position angle offset. The final seeing of the combined exposures is $0''.93$ for KiDS-EC1 and $0''.84$ for KiDS-EC2.

Reduced data have been provided by ESO as Internal Data Products, using the official MUSE pipeline (v2.8). For KiDS-EC1 we have also performed our own data reduction to check consistency with the ESO Phase 3 data products, using the same pipeline. We have found very consistent spectral quality, in terms of flat-fielding, signal-to-noise-ratio (S/N) and sky subtraction. A zoom-in of the FOVs of the EC data cubes (i.e., the integrated flux over all wavelengths) are reported in Figure 1, and clearly show all sources seen in the KiDS *gri* color images (also shown in the same figure). In Figure 1, we also present the 1D spectra from the four lensed images, extracted from a single MUSE pixel, and the one of the corresponding deflector, extracted over an aperture of 3 pixels for KIDS-EC1 and 4 pixels for KIDS-EC2, respectively, corresponding to about half of the effective radius, $R_e/2$, see Section 2.2. We use these apertures because they allow us to minimize the contamination from the blue lensed sources. For both systems, the lensing nature is confirmed by the presence of identical spectral features in the four different images, all consistent with the same redshift, higher than the one of the lens. For KIDS-EC1, we infer a redshift of $z = 1.590 \pm 0.001$ from Fe and Mg absorption lines and faint [FeII] ($\lambda = 5650$Å), [CII] ($\lambda = 6025$Å) and [OII] ($\lambda = 6400$Å) emissions. For KIDS-EC2, we calculate instead $z = 1.102 \pm 0.001$, from the spectrum at $\lambda > 7800$Å, including Balmer absorption lines (H10 at $\lambda \sim 7980$Å, H9 at $\lambda \sim 8060$Å, H8 at $\lambda \sim 8180$Å, Hϵ at $\lambda \sim 8350$Å and Hδ at $\lambda \sim 8620$Å), the calcium K and H doublet (at $\lambda \sim 8360 - 8450$Å), although with some sky contamination in H, and a clear [OII] doublet emission line at $\lambda \sim 7850$Å. In this latter case Fe and Mg absorption lines are also present but look slightly blueshifted, possibly due to some gas outflow from the source galaxy (see e.g., Rubin et al. 2014; Burchett et al. 2020), which we will investigate in a forthcoming paper.

The two deflectors reveal typical features of early-type galaxies (ETGs), in particular a strong rest-frame break at 4000 Å, faint Balmer lines in absorption, and Fe, Mgb, and NaD lines, all characteristic of an old, metal-rich stellar population. The inferred deflector redshifts are $z_l = 0.381 \pm 0.001$ for KIDS-EC1, and $z_l = 0.237 \pm 0.001$ for KIDS-EC2. The S/N and resolution of the spectra allow us to estimate the velocity dispersion of these two systems using

KIDS J232940-340922
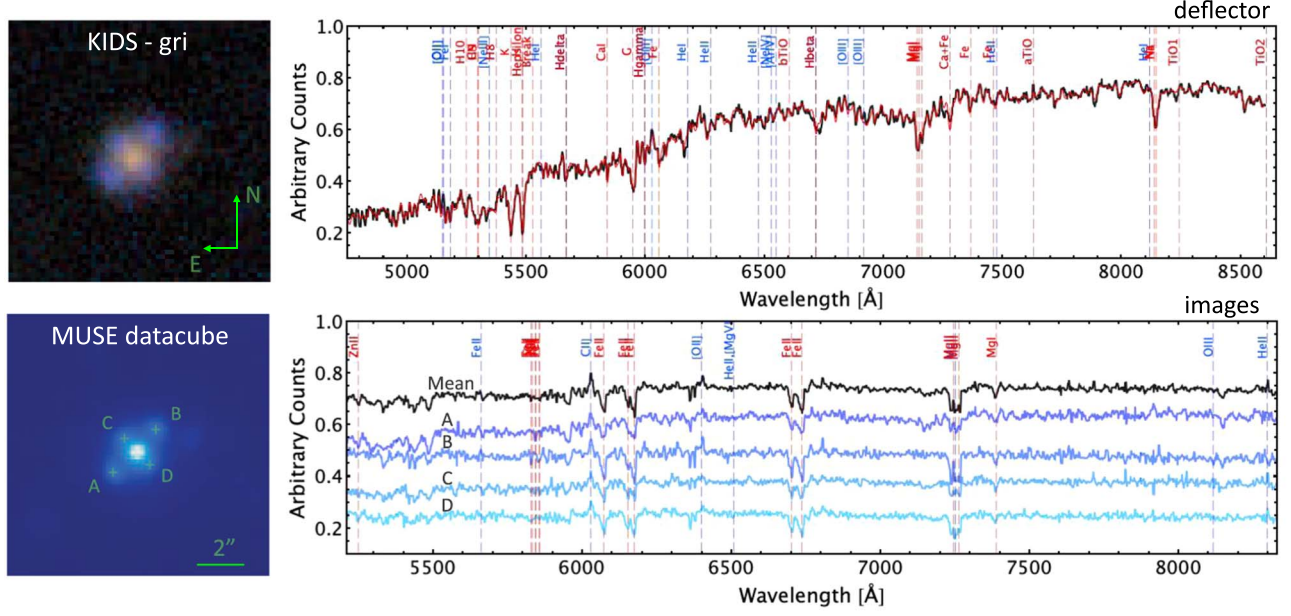
KIDS J122456+005048
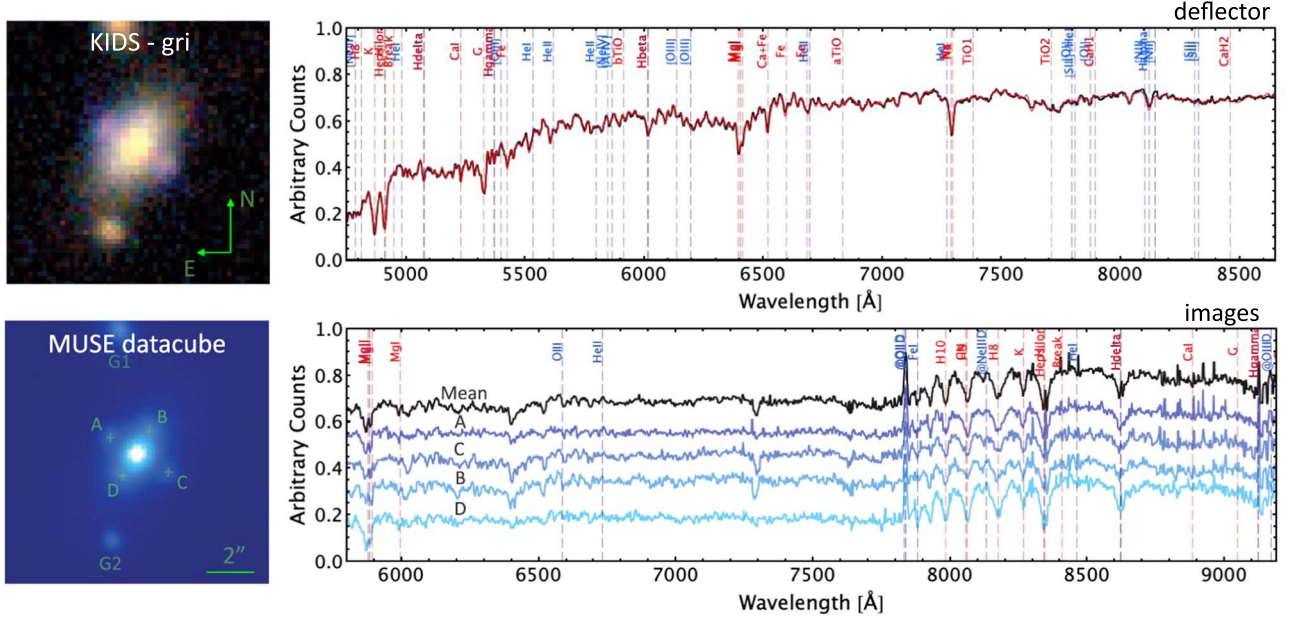
Figure 1. Detection and confirmation of the ECs: KIDS J232940-34092 (top two rows), KIDS J122456+005048 (bottom two rows). Left column: for each cross we show the KiDS (*gri*) color image (top two rows) and the MUSE white light image (bottom two rows). Right column: for each cross we plot the MUSE spectrum of the deflector, in black, with the best-fit model for the velocity dispersion estimate with PPXF, in red, (top two rows) and of the four individual images, in blue tones, and the mean spectrum, in black (bottom two rows). Overplotted on all spectra are the main absorption lines (in red) and emission lines (in blue), shifted to the estimated redshift of the represented object (see Table 2).

the PPXF software (Cappellari 2017), yielding $\sigma_{R_e/2} = 192 \pm 4$ km s^{-1} for KIDS-EC1 and $\sigma_{R_e/2} = 248 \pm 2$ km s^{-1} for KIDS-EC2[22] (see also Table 2). The best-fit models are overlaid on the galaxy spectra in the same Figure 1.

2.2. Lensing Model, Dynamical Masses, and DM Fractions

The two ECs are modeled using the *lfit _gui* code (Shu et al. 2016). We use KiDS $r-$ band images, with a pixel scale of

0″2 and seeing 0″8 for KIDS-EC1 and 0″7 for KIDS-EC2. The effect of the seeing is taken into account by convolving the lensing models with a point-spread function (PSF) generated by nearby stars (see e.g., Roy et al. 2018). The *lfit _gui* code simultaneously models the deflector light, the lensed image positions, and their magnification, and the best position and light distribution of the source galaxy. We assume a single Sérsic profile (Sérsic 1963) for the two deflectors, although for KIDS-EC2 we need to account also for the presence of two nearby galaxies (G1 and G2, respectively, see Figure 1), as well as for the two sources. The deflector total mass distributions are

---

[22] We estimate that systematic errors from template mismatch and masked regions may amount to $\sim$20 km s^{-1}.

Table 1
EC Optical-NIR Photometry

ID	ΔRA (arcsec)	ΔDEC (arcsec)	u (mag)	g (mag)	r (mag)	i (mag)	Z (mag)	Y (mag)	J (mag)	H (mag)	K_s (mag)
KIDS-EC1: KIDS J232940-340922 RA = 352.417753 DEC = −34.156375										
G	0.00 ± 0.03	0.00 ± 0.03	21.44 (0.22)	20.69 (0.09)	19.77 (0.04)	19.29 (0.04)	19.05 (0.12)	18.48 (0.06)	17.90 (0.08)	17.19 (0.08)	16.48 (0.04)
A	−1.04 ± 0.06	−0.75 ± 0.05	22.57 (0.17)	21.97 (0.15)	22.29 (0.11)	22.27 (0.17)	21.16 (0.11)	21.14 (0.14)	20.46 (0.12)	19.70 (0.12)	19.39 (0.12)
B	0.87 ± 0.08	0.99 ± 0.05	22.65 (0.19)	21.98 (0.11)	22.36 (0.12)	22.10 (0.15)	21.32 (0.13)	21.29 (0.17)	20.24 (0.10)	19.60 (0.10)	19.44 (0.12)
C	−0.58 ± 0.09	0.67 ± 0.07	24.06 (0.79)	22.24 (0.17)	22.62 (0.29)	22.23 (0.37)	21.31 (0.24)	21.18 (0.21)	20.38 (0.16)	20.14 (0.23)	20.32 (0.39)
D	0.61 ± 0.19	−0.72 ± 0.16	25.44 (1.65)	22.80 (0.39)	23.14 (0.38)	23.24 (0.51)	21.86 (0.39)	21.81 (0.71)	21.32 (0.42)	20.23 (0.43)	19.57 (0.18)
KIDS-EC2: KIDS J122456+005048 RA = 186.233401 DEC = +0.846682										
G	0.00 ± 0.01	0.00 ± 0.01	20.94 (0.09)	19.30 (0.03)	18.10 (0.03)	17.48 (0.04)	17.20 (0.03)	17.04 (0.05)	16.67 (0.06)	16.24 (0.02)	15.98 (0.38)
A	−1.24 ± 0.05	0.78 ± 0.05	23.13 (0.14)	22.52 (0.16)	21.90 (0.17)	21.57 (0.13)	20.74 (0.08)	20.51 (0.09)	20.34 (0.11)	20.33 (0.08)	19.82 (0.42)
B	0.50 ± 0.07	1.29 ± 0.08	23.25 (0.11)	23.14 (0.33)	22.01 (0.21)	21.79 (0.21)	21.05 (0.09)	20.97 (0.11)	20.66 (0.12)	20.56 (0.09)	19.87 (0.42)
C	1.27 ± 0.06	−0.96 ± 0.06	23.44 (0.15)	22.63 (0.16)	21.97 (0.15)	21.65 (0.13)	20.73 (0.08)	20.62 (0.11)	20.43 (0.11)	20.08 (0.08)	19.96 (0.44)
D	−0.73 ± 0.09	−1.14 ± 0.09	23.36 (0.18)	22.77 (0.29)	22.11 (0.22)	21.93 (0.27)	21.22 (0.15)	21.12 (0.16)	20.94 (0.19)	20.69 (0.10)	20.34 (0.46)

Note. Objects coordinates are in degree, errors on magnitudes in different bands are given in brackets. Magnitudes of the lensed images (A, B, C, D) are total magnitudes obtained by Gaussian fit after the central galaxy G has been removed. Galaxy magnitude are total Sérsic magnitudes.

modeled with an SIE (Kormann et al. 1994) profile with a projected 2D surface mass density profile described by

$$\Sigma(x, y) = \frac{1}{2}\Sigma_c \sqrt{q} \; \theta_E \; (x^2 + q^2 y^2)^{-1/2}, \qquad (1)$$

where θ_E is the lensing strength, equivalent to the Einstein radius, q is the minor-to-major axis ratio of the isodensity contours. $\Sigma_c = c^2/(4\pi G)(D_s/D_d D_{ds})$ is the critical density, where D_s and D_d are the angular diameter distances from the observer of the lens and the source, respectively, and D_{ds}, the distance between deflector and source. The assumption of an SIE model is motivated by evidence pointing toward a logarithmic mass-density slope close to −2 for the total mass density around the Einstein radius (e.g., Koopmans et al. 2006); however, the impact of this assumption is discussed in the Appendix, while a full modeling with more general density profiles will be presented in future detailed analyses. We also include external shear, γ_{ext}, which approximates the influence of the surrounding environment on the lensing potential. After having initialized the model, with some test runs, the final best-fit of the two ECs are obtained via χ^2 minimization using the Levenberg-Marquardt algorithm (Moré 1978). These are shown in Figure 2, and the corresponding parameters are reported in Table 2. From the Table, we can draw some first general results: (1) the two ECs show similar Einstein radii, R_E, which are both very close to the lens effective radii, R_e (i.e., $R_E/R_e \sim 0.9$); (2) the stellar velocity dispersion measured from the spectrum of KIDS-EC1 is smaller than that inferred by the lens model, suggesting that the actual slope of the total density profile might deviate from −2 (see, e.g., Auger et al. 2010 and

the discussion in the Appendix), while the two values are consistent within 2σ for KIDS-EC2; (3) for both lenses, the total mass may be rounder than the starlight distribution (i.e., $b/a = 0.91$ versus 0.89 for KIDS-EC1 and $b/a = 0.68$ versus 0.59 for KIDS-EC2), but consistent within the errors, as earlier found in other studies (e.g., Shajib et al. 2020 and reference therein); (4) for KIDS-EC1 we measure a quite strong external shear ($\gamma_{ext} \sim 0.25$), compatible with a group/cluster potential, which is confirmed by the presence of 12 more galaxies at a similar redshift as the lens within 30″ distance in the MUSE FOV (N. R. Napolitano et al., in preparation); (5) both sources are aligned with the lens center of mass within 0″.1, while the stellar and mass centers are consistent within the errors. In the Appendix we discuss the impact of more general model density assumptions and show that these do not impact the main conclusions of this study. From the lens model parameters, we infer a projected mass within R_E of $\log M(R_E)/M_\odot = 11.28 \pm 0.02$ for KIDS-EC1 and $\log M(R_E)/M_\odot = 11.42 \pm 0.01$ for KIDS-EC2 (see also Table 2). Due to the underlying assumption of an SIE mass distribution, we can easily derive the mass inside $R_e/2$ (i.e., $M(R_e/2)$ in Table 2) to compare with the dynamical mass by the velocity dispersion measurements inside the same radius, derived above. We remark here that the adoption of $R_e/2$ as reference radius is consistent with previous strong lensing studies at the same scale (e.g., Auger et al. 2010).

For the dynamical masses, we use the projected solution of the Jeans Equation inside a circular aperture (e.g., Tortora et al. 2009), in order to take correctly into account the light profile of

Table 2
Summary of the EC Main Parameters

Parameter	KIDS-EC1	KIDS-EC2
MUSE Spectroscopy		
z_l	0.3810 ± 0.001	0.2372 ± 0.0005
z_s	1.59 ± 0.01	1.10 ± 0.01
$\sigma_{R_e/2}$ (km s^{-1})	192 ± 4	248 ± 5
Lensing Model		
θ_E (arcsec)	0.99 ± 0.02	1.42 ± 0.01
R_E (kpc)	5.2 ± 0.1	5.4 ± 0.1
σ_E (km s^{-1})	226 ± 8	260 ± 5
lens b/a	0.91 ± 0.07	0.68 ± 0.07
lens PA	1 ± 56	148 ± 2
μ_r (A, B, C, D)	(3.6, 3.4, 2.7, 1.7)	(5.6, 5.1, 5.3, 4.6)
lens PA	1 ± 56	148 ± 2
star n −index	2.8 ± 0.3	3.43 ± 0.08
star b/a	0.89 ± 0.03	0.59 ± 0.01
star PA	107 ± 9	146 ± 1
star R_e (arcsec)	1.12 ± 0.10	1.63 ± 0.05
star R_e (kpc)	5.8 ± 0.5	6.2 ± 0.2
R_E/R_e	0.90 ± 0.08	0.87 ± 0.03
star Δ RA	-0.02 ± 0.02	0.01 ± 0.01
star Δ DEC	0.02 ± 0.02	0.01 ± 0.01
source n −index	0.4 ± 0.1	0.2 ± 0.1
source b/a	0.5 ± 0.1	0.7 ± 0.1
source R_e (arcsec)	0.10 ± 0.02	0.06 ± 0.01
source R_e (kpc)	0.87 ± 0.14	0.46 ± 0.04
source ΔRA	-0.03 ± 0.02	0.04 ± 0.01
source ΔDEC	-0.07 ± 0.02	0.05 ± 0.01
external shear γ_{ex}	0.25 ± 0.03	0.01 ± 0.01
Mass Estimates		
$\log M(R_E)/M_\odot$	11.28 ± 0.02	11.42 ± 0.01
$\log M(R_e/2)/M_\odot$	11.04 ± 0.03	11.18 ± 0.01
$\log M_J(R_e/2)/M_\odot$	10.95 ± 0.05	11.21 ± 0.02
$\log M_*/M_\odot$	11.18 ± 0.04	11.33 ± 0.03
$\log M_*/M_\odot(R_e/2)$	10.65 ± 0.04	10.81 ± 0.03
$f_{DM}(R_e/2)$	0.60 ± 0.07	0.56 ± 0.04
$\Delta f_{DM} = f_{DM,len} - f_{DM,J}$	0.09 ± 0.10	-0.02 ± 0.07

Note. EC parameters. MUSE spectroscopy: redshift of the lens and source and velocity dispersion of the lens calculated at $R_e/2$. Lensing models: Einstein radius in arcsec (θ_E) and kpc (R_E) and the model SIE velocity dispersion, σ_E, followed by self-explaining parameters related to the total mass (labeled by "lens"), stellar mass parameters (labeled by "star"), and source parameters (labeled by "source") light distribution. Offsets (ΔRA, ΔDEC) are calculated with respect to the lens center. Mass estimates: summary of the mass estimates from lensing model (M), Jeans model (M_J), and stellar population M_* (see the text for details) together with the projected DM fractions (f_{DM}) and difference between lens ($f_{DM,len}$) and Jeans ($f_{DM,J}$) analyses.

the lenses (i.e., n −index).[23] These projected masses, M_J in Table 2, are fully consistent with the equivalent lensing-derived masses, hence confirming the self-consistency of our mass estimates of the two systems.

We finally estimate the total stellar mass, M_*, of the two lens systems via SED fitting of the nine-band photometry, given in Table 1. We use the public SED fitting-Code Investigating GALaxy Emission (CIGALE v2018.0; Boquien

et al. 2019. The M_*, are used, in combination with the lensing masses, to derive the DM fraction inside $Re/2$, $f_{DM} = 1 - M_*(R_e/2)/M(R_e/2)$. We assume solar metallicity, while all other parameters, such as the e-folding time, age of the main stellar population, and internal extinction, E(B-V), are free to vary. For the star formation rate (SFR), we adopt a delayed star formation history, which allows us to efficiently model both typical ETGs and late-type galaxies (see Boquien et al. 2019). To double check the results we also use another independent code, LE PHARE (Ilbert et al. 2006), with a similar set-up and found consistent results for all the constrained parameters, within the errors. The stellar mass inside $R_e/2$ is derived assuming a constant stellar mass-to-light ratio for each lens Sérsic light profile, whose parameters have been inferred from the lensing model in Table 2. The final estimates of $M_*(R_e/2)$ are reported in the same Table, where we also list the final $f_{DM} = 0.60 \pm 0.07$ for KIDS-EC1 and $f_{DM} = 0.56 \pm 0.04$ for KIDS-EC2, and report the difference between the lensing and dynamical DM fractions (Δf_{DM}).

The inferred f_{DM} are typical of DM-dominated systems and consistent with previous estimates based on lensing (Auger et al. 2010; Tortora et al. 2010; Schuldt et al. 2019) or dynamics of local (Tortora et al. 2009; Cappellari et al. 2012; Tortora et al. 2012) or higher redshift galaxies (Beifiori et al. 2014; Tortora et al. 2018) of similar stellar masses.

3. Characterization of the Sources

A striking outcome of the lensing model is the degree of compactness of the source galaxies in both ECs, that turned out to have effective radii smaller than $0.''1$. The lensing model also provides an estimate of the n-indexes (<1 in both cases) and axis ratios (~0.9 and ~0.6, respectively), suggesting that the two sources might be disk-dominated systems.[24] Only space or adaptive-optics imaging will provide accurate constraints for these parameters and confirm these findings, but meanwhile, to better assess the reliability of the ground-based inferences, we test the procedure using 20 mock ECs. We follow the same approach used to simulate the lensing systems centered on randomly selected red luminous galaxies used to train our CNN on KiDS ground-based images (see Li+20). In particular, we produce quad configurations using a source effective radius varying between $R_e = [0.''05, 0.''15]$, n-index $= [0.05, 2]$, lens effective radius $R_e = [1.''0, 1.5'']$, and Einstein radius, $R_E = [1.''0, 1.''5]$. The ranges adopted are meant to cover the parameter space embracing the two crosses, and to demonstrate that the lens model tool can recover the parameters correctly. In particular, we have tested the case of very small R_e and n-index of the source by modeling 4/20 mock lenses with $R_e < 0.''07$ and n −index < 0.6. The simulated lenses are then convolved with a typical r − band PSF of KiDS observations and noise is finally added to produce realistic KiDS-like r-band EC images. We then run the *lfit _gui* using the same configuration file on these mock ECs and derived the lensing parameters like for the real ECs. The derived source R_e and n-index fall on the one-to-one relation with the input ones. To quantify this we derive the following quantities: $\Delta R_e/R_e = (R_{e, in} - R_{e, out})/R_{e, in} = -0.01 \pm 0.06$ and

---

[23] This is the most accurate way to determine the mass inside an aperture and avoid assumptions about the virial estimates for a non-de Vaucouleurs profile ($n \neq 4$), see, e.g., Cappellari et al. (2006).

[24] The best-fit n-indexes are fairly small if compared to typical disks: however, we have checked that fixing $n = 1$, the other parameters change within the errors and the reduced χ^2 is worsened, hence demonstrating that n-indexes are realistically $\lesssim 1$ (see, e.g., former findings on lensed quenching galaxies by Geier et al. 2013).
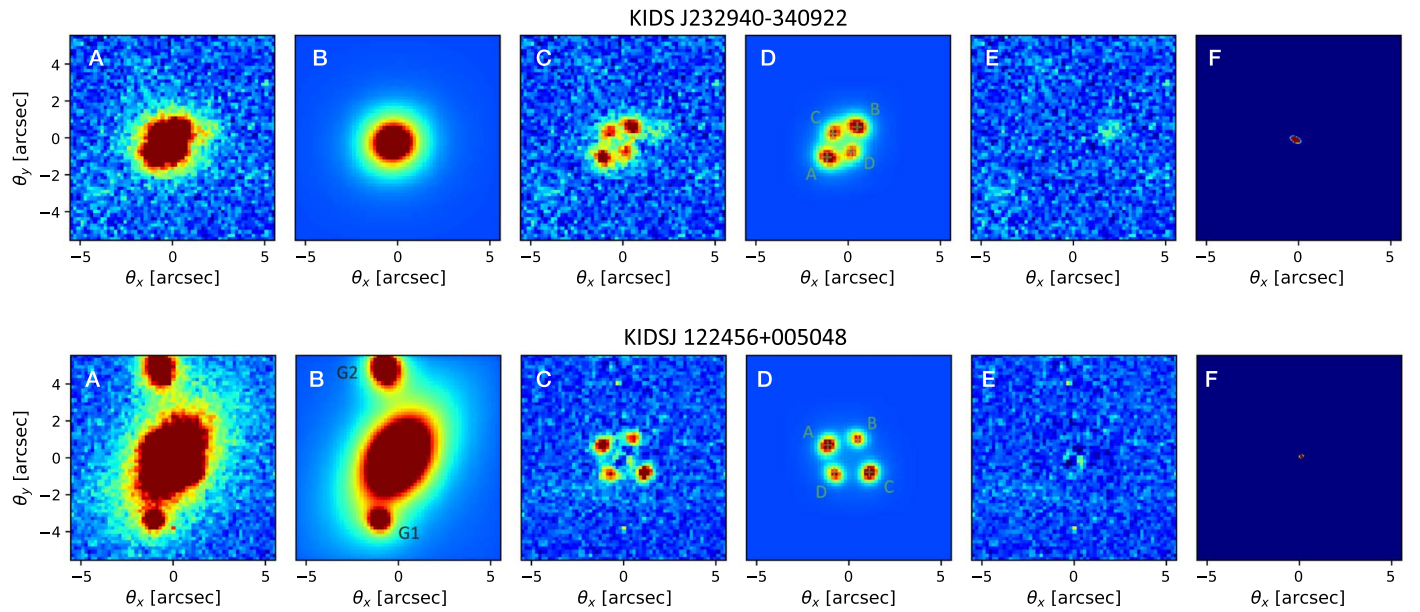
Figure 2. Lensing models for KIDS J232940-34092 (top row), KIDS J122456+005048 (bottom row). From left to right we show the r−band KiDS image used for the model (A), the foreground light-subtracted image (B), the EC images with the foreground light subtracted (C), the reconstructed ECs, the residual image ($E = A−B−D$), and the reconstructed background source (F). We use an SIE to model the deflector mass model and a Sérsic model for foreground and source light. For KIDS J122456+005048, to model the foreground light, we also account for the light of the two nearby galaxies marked as G1 and G2 (see panel B). They are also visible in the KiDS and MUSE images (see Figure 1) and found to have a similar redshift as the lens.

$\Delta n/n = (n_{in} - n_{out})/n_{in} = -0.01 \pm 0.15$. The scatter is even smaller (~0.03 both in R_e and n) for the four most extreme cases. Because they are both consistent with zero and the (1σ) scatter is consistent with typical errors from the best-fit parameters in Table 2 ($\lesssim 20\%$), we are confident that the "compactness" of the sources as well as its "disk-like" nature are real, although for the latter there might be more freedom about the exact value of the n-index. We also note that sub-pixel sizes of the sources are referenced to the source plane, where *lfit _gui* maps the source model with a spatial resolution $10\times$ higher than the pixel scale of the lens plane, where the source images are observed ($0.''2$ for KiDS images). Hence, sizes that are smaller than a single pixel are well within the reach of the tool that we use. However, we have found that $0.''04$ is the lowest limit for our ground-based observations. In fact, mock lenses that have sources with R_e in the range [0.01, 0.04] are recovered with uncertainties that are too large.

As described in Section 2.1, the source spectra are dominated by absorption lines that are typical of a relatively evolved population, and show only weak emission lines (see Figure 1), which is somehow at odds with the blue colors produced by their continuum. In particular, KIDS-EC1 shows a low-S/N [OII] emission, while KIDS-EC2 shows [OII] and Hϵ, Hδ, and Hγ Balmer lines in emission, although the latter are superimposed to absorption Balmer lines, which makes any modeling of their profile very degenerate (e.g., continuum level, velocity dispersion of the absorption, and emission lines, age, metallicity). Using the [OII] line, after some careful continuum subtraction, we estimate a tentative SFR of $\sim 0.1 M_\odot$ yr^{-1} (using Equation (3) in Kennicutt 1998). We stress that a S/N ~ 6 is not high enough for a robust estimate.

To better characterize the nature of the two sources, we thus exploit their nine-band photometry (Table 1) and run CIGALE, as already done for the deflectors. In order to increase the S/N of the source SEDs, we average the fluxes of the higher magnified lensed images (AB for KIDS-EC1 and AC for

KIDS-EC2) and obtain the de-lensed (i.e., using the r−band magnification, μ_r, as in Table 2) SED in Figure 3. We try two extreme metallicity scenarios: a standard solar metallicity and a largely sub-solar one ($Z = 0.0004$), the latter being suggested by the strength of the Balmer lines compared with the calcium H and K of KIDS-EC2 (for EC1 these lines are too redshifted to fall in the MUSE wavelength range). For KIDS-EC1 we obtain a better fit with solar metallicity (reduced $\chi^2 = 1.7$, corresponding to a ~10% significance for 8 degrees of freedom), while for EC2 the fit is better for the sub-solar metallicity ($\chi^2 = 0.7$, i.e., ~70% significance). The best fits, shown in Figure 3, give for KIDS-EC1 an age of 4.0 ± 0.1 Gyr and an SFR of $9.1 \pm 1.2 M_\odot$ yr^{-1}, while for for KIDS-EC2, age $= 3.8 \pm 0.4$ Gyr and SFR $= 0.4 \pm 0.1 M_\odot$ yr^{-1}.[25] Hence, both systems are old for their redshift but they are still forming stars at a low rate, although we see only few emission lines in their spectra. In both cases the sources are quite massive: KIDS-EC1 has a stellar mass of $\log M_*/M_\odot = 11.08^{+0.04}_{-0.05}$ and KIDS-EC2 of $\log M_*/M_\odot = 10.21^{+0.02}_{-0.02}$, hence their specific star formation rate (sSFR) are $\log sSFR/Gyr = -1.12 \pm 0.07$ and $\log sSFR/Gyr = -1.61 \pm 0.03$, respectively, i.e., generally lower than the the typical values expected for the main sequence (MS) of star-forming (SF) galaxies at $z > 1$ in the same mass range ($\log sSFR_{MS}/Gyr \sim 0.0 \pm 0.4$, see e.g., Johnston et al. 2015).

For the lensed images we have also performed a double check with LE PHARE and we have found slightly lower masses (0.1 and 0.2 dex for KIDS-EC1 and EC2, respectively) that are consistent or even lower $\log sSFR/Gyr$ (-1.3 and -1,

---

[25] For completeness, the results obtained for KIDS-EC1 assuming a sub-solar metallicity are age $= 4.0 \pm 1.0$ Gyr and SFR $= 0.4 \pm 0.1 M_\odot$ yr^{-1} and the results for KIDS-EC2 with solar metallicity are age $= 1.2 \pm 0.2$ Gyr and SFR $= 5.5 \pm 0.3 M_\odot$ yr^{-1}. Note that full spectro-photometric stellar population analysis of the sources is beyond the scope of this Letter and will be addressed in a separate paper.
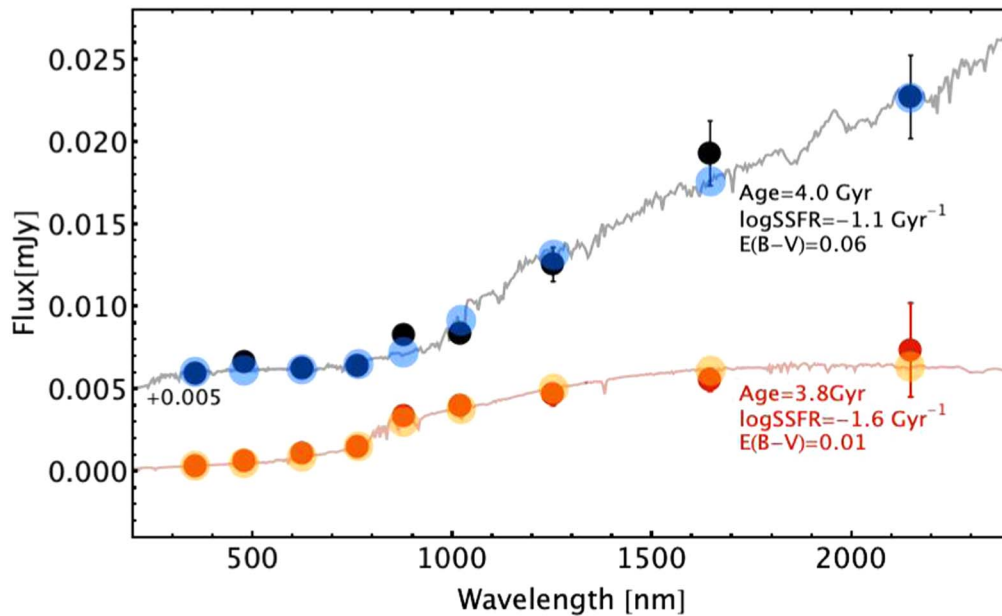
Figure 3. SED fitting of the mean optical+NIR photometry obtained from averaging the de-lensed fluxes of the most magnified images in Table 1. KIDS J232940-34092 photometry (black points with errorbars) is plotted together with the best-fit template model (solid gray line), corresponding to the parameters reported in the figure (see the text for more details) and solar metallicity. Dark blue points show the corresponding photometry from the model used to fit the observations. KIDS J122456+005048 photometry (red points with errorbars) is plotted against the best-fit model (light red line) and integrated photometry (yellow points), as well as model parameters for the sub-solar metallicity case (see the text for details). Data from KIDS J232940-34092 have been shifted +0.005 upward for clarity.

respectively), hence confirming the quenching status of the two systems.

Are these systems special? They are for their sizes, as they are both outliers of the typical size–mass relation of SF systems by ∼0.5dex in effective radius. For instance, Allen et al. (2017) found a mean $\log R_e/$kpc ∼0.6 and 0.5 in the redshift bin $1 < z < 1.5$ for $\log M_*/M_\odot \sim 11.1$ and ∼10.2, respectively, while we have $\log R_e/$kpc $= -0.06$ for KIDS-EC1 and -0.34 for KIDS-EC2. This means that they deviate significantly from normal galaxies at their redshift, while they are closer to typical sizes of SF galaxies at $z \gtrsim 5$. On the other hand, they also show very low sSFR, deviating from the MS by $\Delta_{MS} = \log$ sSFR$_{MS} - \log$sSFR ~ -1.1 and -0.4. Simulations from Tacchella et al. (2016) have shown that these low sSFRs, together with sizes of $\log R_e/$kpc < 0, are typical of a "post-blue nugget" (BNs) phase, i.e., systems that have gone through compaction and have entered their quenching phase. Huertas-Company et al. (2018) have also found that most of the massive, compact systems at z > 1 ($\log M_*/M_\odot \gtrsim 10.3$) tend to be in such a post-BN phase.

4. Conclusions and Perspectives

We have presented the confirmation and modeling of two ECs found in the KiDS footprint. The confirmation is based on MUSE spectroscopy, unequivocally showing the strong-lensing nature of the systems. We have detected the same spectral features in the four images of the two crosses and inferred a redshift of $z_s \sim 1.59$ for KIDS-EC1 and $z_s \sim 1.10$ for KIDS-EC2, both higher that their respective deflector galaxies, i.e., two old ETGs at $z_l \sim 0.38$ (KIDS J232940-340922) and $z_l \sim 0.24$ (KIDS J122456+005048).

The discovery is exceptional as we only inspected ∼1000deg^2 so far and ECs are very rare phenomena. However, general predictions on the number of expected quads (of which ECs are a special case) are based on the assumption that these

are generated by quasars (see e.g., Oguri & Marshall 2010). For the two ECs presented here, we have shown that they are produced by ultra-compact, blue, quenching galaxies. In particular:

1. to reproduce the cross configuration, the best lensing model (see Table 2), assuming an SIE with external shear, predicts that the sources have very compact sizes: $R_e \sim 0.9$ kpc for KiDS-EC1 and $R_e \sim 0.5$ kpc for KiDS-EC2, i.e., $>10\sigma$ off the typical size–mass relation of normal SF galaxies at the same redshifts (see Allen et al. 2017);

2. the spectra of the sources show a dominance of absorption lines, typical of a quite evolved stellar population, which has been confirmed by SED fitting of the nine-band photometry performed on the average of the two highest magnified images of each system. We inferred old ages (4 Gyr and 3.8 Gyr for KIDS-EC1 and KIDS-EC2, respectively) and moderate SF (9.1 and 0.4 $M_\odot$ yr^{-1}, respectively). However, the inferred stellar masses ($\log M_*/M_\odot \sim 11.08$ and 10.21, respectively) imply very low specific SFRs ($\log$sSFR $= -1.1$ and -1.6 Gyr^{-1}, respectively), typical of quenching galaxies at $z > 1$ (see e.g., Tacchella et al. 2016; Newman et al. 2018).

In Section 3, we have argued that the combination of an extremely compact size and the low sSFR is compatible with the sources being two massive post-BNs. These are compact massive galaxies have almost exhausted their star-forming phase and are currently undergoing quenching. As such, these systems are important for understanding the transformation of primordial disks into the compact cores ("red nuggets;" see Dekel & Burkert 2014) of today's large elliptical galaxies in the first phase of their evolution, before they enter their subsequent merging phase (e.g., Oser et al. 2012). These systems have been predicted to be very numerous in simulations (e.g.,

Zolotov et al. 2015; Tacchella et al. 2016) and their census at $z > 1$ has just started, including the confirmation of their abundance and physical properties (see e.g., Huertas-Company et al. 2018). The fact that there are two such systems in a peculiar lensing configuration might suggest that, indeed, they are not uncommon at $z > 1$. To make a rough estimate of the expected numbers of such EC events from compact post-BN systems, we can use predictions based on a size–luminosity relation compatible with high-z studies calibrated over compact SF galaxies from Collett (2015), reproducing typical ground-based surveys with seeing $\leqslant 1''$.[26] We estimate ~ 1 EC over $1000 \deg^2$ (assuming $< 0''\!.1$ alignment between source and deflector), generated by a slightly flattened mass distribution like the one estimated for our ECs ($q = [0.7, 0.9]$) by a compact source (size $\lesssim 1$ kpc) at $z < 1.7$, with sufficient S/N (>10) to be identified as a sure lens around bright deflectors ($r < 21$, according to our selection in Li+20). This rough prediction can be likely an upper limit because we are assuming that all sources aligned within $0''\!.1$ produce an EC; however, by using mock lenses we have confirmed that most of them should look this way (see Section 3). The two ECs reported here are possibly slightly overabundant with respect to the expectation for standard SF systems. This is the first interesting indication that this population of post-BNs might be particularly abundant at $z > 1$. According to the same predictions, releasing any limitation on the brightness of the lens (i.e., $r < 25$), the expected EC/quad configurations are $\sim$half a dozen for sources at $z < 4$ (see also Section 1). Hence, in the future we expect to confirm other systems in KiDS. More importantly, we can expect that for next-generation surveys like the Vera C. Rubin Observatory (previously referred to as the Large Synoptic Survey Telescope), Euclid, or the China Space Station Telescope, we can discover 4000 to 7000 similar quad-like configurations. This will provide a unique opportunity to perform systematic studies of this population of compact systems in great detail using lensing as a "gravitational telescope," which would be very difficult to observe without lensing magnification (see, e.g., Toft et al. 2017) before extremely large telescopes will be online.

Appendix
Impact of the SIE Assumption and the Fitting Tool

The mismatch between the stellar velocity dispersion measured from the spectrum and the lensing dispersion of KIDS-EC1 found in Section 2.2 suggests that the assumption of a SIE mass density might be inappropriate. To investigate the impact of this assumption and check the reliability of the main parameters derived by *lfit_gui* and reported in Table 2, we use a different lens model tool, LENSED (Tessore et al. 2016). We stress that a full comparison of different fitting techniques is beyond the purpose of this Letter; however, we can use the relevant outputs of an independent tool to validate the main results of this paper. First, as LENSED allows a free slope for the mass density profile (i.e., an Elliptic Power Law (EPL) model), we can check how this deviates from SIE (3D slope = 2). For KIDS-EC1 we find the best-fit 3D slope $= -1.75 \pm 0.06$, which is consistent with the Auger et al. (2010) formula ($\gamma' - 2 = 2.67(f_{SIE} - 1) + 0.20$, where γ' is the 3D slope and $f_{SIE} = \sigma_{e/2}/\sigma_{SIE}$) for the mismatch between stellar velocity dispersion measured from the spectrum and the lensing dispersion for the SIE model. For EC2 we have a 3D slope $= 2.04 \pm 0.01$, which is instead very close to the 3D slope predicted for an SIE. Due to the different slopes, we derive different 2D mass extrapolation at $R_e/2$: for KIDS-EC1 we have $\log M(R_e/2)/M_\odot = 10.99 \pm 0.07$, for KIDS-EC2 we have $\log M(R_e/2)/M_\odot = 11.20 \pm 0.02$. The inferred DM fractions are $f_{DM} = 0.54 \pm 0.11$ for KIDS-EC1 and $f_{DM} = 0.58 \pm 0.05$ for KIDS-EC2, i.e., fully consistent with the SIE results within 1σ. This shows that the inner slope does not impact significantly our inference on the DM content of the galaxies, as well as the overall conclusions related to the lensing parameters in Table 2, hence the use of the SIE in the rest of this Letter is fairly justified.

Another central result of this Letter is the compactness of the source, which, as discussed in Section 3, is challenging to assess from ground-based imaging and might depend, e.g., on the way a given tool samples the model at the sub-pixel scale, performs the convolution with the PSF, and re-bins the model. We have double checked the results of *lfit_gui* against LENSED and confirmed both compactness and the pseudo-exponential light profiles of the sources, even though the central values are consistent only within $\sim 2\sigma$. In fact, from LENSED we found that the source sizes of KIDS-EC1 is $R_e = 0.05'' \pm 0''\!.01$ while its n-index is $n = 1.2 \pm 0.3$; for KIDS-EC2, we found instead $R_e = 0.03'' \pm 0''\!.01$ and $n = 1.58 \pm 0.07$. Finally, source axis ratios and magnitudes

---

[26] We have used the pre-compiled predictions for the Dark Energy Survey (DES), with seeing $1''$ in github.com/tcollett/LensPop. These simulations are consistent with KiDS in terms of depth ($r \sim 25$, 5σ within $2''$), hence giving access to a similar lens luminosity distribution, and only slightly worse in image quality ($\sim 1''$ for DES versus $0''\!.7$ for KiDS and a pixel size $0''\!.26$ versus $0''\!.21$). Furthermore, the adoption of a slightly larger seeing allows us to better account for the selection function introduced by the visual inspection, as the human eye tends to give a lower-grade to arcs or multiple images that are too close to the lens center as they look diluted/confused in the lens starlight.

are fairly similar to *lfit_gui* inferences: for KiDS-EC1, LENSED gives $(b/a, r) = (0.24, 23.54)$, for KiDS-EC2 $(0.64, 23.80)$. As a comparison, *lfit_gui* gives $(0.5, 23.78)$, $(0.7, 23.69)$ for KiDS-EC1 and KiDS-EC2, respectively.

ORCID iDs

N. R. Napolitano ⓘ https://orcid.org/0000-0003-0911-8884
R. Li ⓘ https://orcid.org/0000-0002-3490-4089
C. Spiniello ⓘ https://orcid.org/0000-0002-3909-6359
C. Tortora ⓘ https://orcid.org/0000-0001-7958-6531
A. Sergeyev ⓘ https://orcid.org/0000-0003-3425-5178
G. D'Ago ⓘ https://orcid.org/0000-0001-9697-7331
X. Guo ⓘ https://orcid.org/0000-0002-2338-7709
L. Xie ⓘ https://orcid.org/0000-0002-2831-8630
M. Radovich ⓘ https://orcid.org/0000-0002-3585-866X
L. V. E. Koopmans ⓘ https://orcid.org/0000-0003-1840-0312
K. Kuijken ⓘ https://orcid.org/0000-0002-3827-0175
M. Bilicki ⓘ https://orcid.org/0000-0002-3910-5809
C. Moya ⓘ https://orcid.org/0000-0002-8876-267X
H. Y. Shan ⓘ https://orcid.org/0000-0001-8534-837X
A. H. Wright ⓘ https://orcid.org/0000-0001-7363-7932

References

Allen, R. J., Kacprzak, G. G., Glazebrook, K., et al. 2017, ApJL, 834, L11
Auger, M. W., Treu, T., Bolton, A. S., et al. 2010, ApJ, 724, 511
Beifiori, A., Thomas, D., Maraston, C., et al. 2014, ApJ, 789, 92
Bettoni, D., Falomo, R., Scarpa, R., et al. 2019, ApJL, 873, L14
Bolton, A. S., Moustakas, L. A., Stern, D., et al. 2006, ApJL, 646, L45
Boquien, M., Burgarella, D., Roehlly, Y., et al. 2019, A&A, 622, A103
Burchett, J. N., Rubin, K. H. R., Prochaska, J. X., et al. 2020, arXiv:2005.03017
Cappellari, M. 2017, MNRAS, 466, 798
Cappellari, M., Bacon, R., Bureau, M., et al. 2006, MNRAS, 366, 1126
Cappellari, M., McDermid, R. M., Alatalo, K., et al. 2012, Natur, 484, 485
Collett, T. E. 2015, ApJ, 811, 20
de Jong, J. T. A., Kuijken, K., Applegate, D., et al. 2013, Msngr, 154, 44
Dekel, A., & Burkert, A. 2014, MNRAS, 438, 1870
Edge, A., Sutherland, W., Kuijken, K., et al. 2013, Msngr, 154, 32
Geier, S., Richard, J., Man, A. W. S., et al. 2013, ApJ, 777, 87
Huertas-Company, M., Primack, J. R., Dekel, A., et al. 2018, ApJ, 858, 114
Ilbert, O., Arnouts, S., McCracken, H. J., et al. 2006, A&A, 457, 841
Johnston, R., Vaccari, M., Jarvis, M., et al. 2015, MNRAS, 453, 2540
Kelly, P. L., Rodney, S. A., Treu, T., et al. 2015, Sci, 347, 1123
Kennicutt, R. C. 1998, ARA&A, 36, 189
Koopmans, L. V. E., Treu, T., Bolton, A. S., et al. 2006, ApJ, 649, 599
Kormann, R., Schneider, P., & Bartelmann, M. 1994, A&A, 284, 285
Kuijken, K., Heymans, C., Dvornik, A., et al. 2019, A&A, 625, A2
Li, R., Napolitano, N. R., Tortora, C., et al. 2020, ApJ, 899, 30, (Li+20)
Magain, P., Surdej, J., Swings, J.-P., et al. 1988, Natur, 334, 325
Moré, J. J. 1978, Lecture Notes in Mathematics (Berlin: Springer), 105
Muzzin, A., Labbé, I., Franx, M., et al. 2012, ApJ, 761, 142
Newman, A. B., Belli, S., Ellis, R. S., et al. 2018, ApJ, 862, 125
Nightingale, J. W., Massey, R. J., Harvey, D. R., et al. 2019, MNRAS, 489, 2049
Oguri, M., & Marshall, P. J. 2010, MNRAS, 405, 2579
Oser, L., Naab, T., Ostriker, J. P., et al. 2012, ApJ, 744, 63
Ostrovski, F., Lemon, C. A., Auger, M. W., et al. 2018, MNRAS, 473, L116
Petrillo, C. E., Tortora, C., Chatterjee, S., et al. 2017, MNRAS, 472, 1129
Petrillo, C. E., Tortora, C., Chatterjee, S., et al. 2019a, MNRAS, 482, 807
Petrillo, C. E., Tortora, C., Vernardos, G., et al. 2019b, MNRAS, 484, 3879
Roy, N., Napolitano, N. R., La Barbera, F., et al. 2018, MNRAS, 480, 1057
Rubin, K. H. R., Prochaska, J. X., Koo, D. C., et al. 2014, ApJ, 794, 156
Schuldt, S., Chirivì, G., Suyu, S. H., et al. 2019, A&A, 631, A40
Sérsic, J. L. 1963, BAAA, 6, 41
Shajib, A. J., Treu, T., Birrer, S., et al. 2020, arXiv:2008.11724
Shu, Y., Bolton, A. S., Mao, S., et al. 2016, ApJ, 833, 264
Spiniello, C., Agnello, A., Napolitano, N. R., et al. 2018, MNRAS, 480, 1163
Spiniello, C., Agnello, A., Sergeyev, A. V., et al. 2019, MNRAS, 483, 3888
Spiniello, C., Koopmans, L. V. E., Trager, S. C., et al. 2011, MNRAS, 417, 3000
Suyu, S. H., Auger, M. W., Hilbert, S., et al. 2013, ApJ, 766, 70
Tacchella, S., Dekel, A., Carollo, C. M., et al. 2016, MNRAS, 457, 2790
Tessore, N., Bellagamba, F., & Metcalf, R. B. 2016, MNRAS, 463, 3115
Toft, S., Zabl, J., Richard, J., et al. 2017, Natur, 546, 510
Tortora, C., La Barbera, F., Napolitano, N. R., et al. 2012, MNRAS, 425, 577
Tortora, C., Napolitano, N. R., Romanowsky, A. J., et al. 2009, MNRAS, 396, 1132
Tortora, C., Napolitano, N. R., Romanowsky, A. J., et al. 2010, ApJL, 721, L1
Tortora, C., Napolitano, N. R., Roy, N., et al. 2018, MNRAS, 473, 969
Treu, T., Auger, M. W., Koopmans, L. V. E., et al. 2010, ApJ, 709, 1195
Zolotov, A., Dekel, A., Mandelker, N., et al. 2015, MNRAS, 450, 2327